Acta Mech
https://doi.org/10.1007/s00707-026-04626-4

ORIGINAL PAPER

Santanu Kumar Sahoo · Nathanaël Machicoane

Two-phase flow turbulence in swirling sprays from a coaxial atomizer

Received: 31 August 2025 / Revised: 18 December 2025 / Accepted: 9 January 2026

Abstract The present investigation focuses on the turbulent characteristics of swirling/non-swirling sprays from a coaxial atomizer. The probability distribution functions of the velocity fluctuation are found to narrow their range with an increase in swirl, for the axial, radial, and tangential components. The centerline gas jet velocity close to the nozzle is observed to be higher in the presence of spray than without it, and while the opposite is true far away from the nozzle. When considering the carrier phase, the axial velocity fluctuations show self-similar radial profiles independently of the spray parameters. The droplets, on the other hand, display off-center maxima, except for low-swirling sprays, at a high gas-to-liquid dynamic pressure ratio M. On the contrary, only the latter conditions have off-centered maxima for the droplet radial velocity fluctuations. Although an expected self-similarity is observed for the Reynolds stress term $\langle uv \rangle$ for the gas phase, the droplet covariance is found to increase with swirl. The behaviors of the other terms, including the gas Reynolds stresses and the droplet covariances, are also characterized in detail, along variations of M and swirl in particular. Furthermore, the gas flow's integral time scale is observed to increase, while the dissipation rate decreases with an increase in swirl. The computation of the local Stokes number highlights the difficulty in finding adequate seeding material to faithfully be tracers of such high-speed sprays. This comprehensive database of spray turbulence can serve in future spray models.

1 Introduction

The disintegration of a liquid jet or sheet into droplets, called atomization, is undertaken to increase the liquid surface area for enhancing different transfer processes. The resulting collection of droplets is known as a spray. Industrially, they are relevant for various purposes such as fuel sprays in the field of combustion science [1,2], liquid metal spray for powder production for additive manufacturing [3,4], pesticide spray for agricultural use, spray for coating in the pharmaceutical industry [5], among many others. In order to achieve the production of these sprays, different industries adopt need-specific methods, some of which are shown in Fig. 1. For example, while sprays produced from the fragmentation of swirling liquid sheets are used for gas turbine engines [6], the rocket engines often implement gas-assisted liquid jet breakup [7]. The breakup of bulk liquid in atomizers is a result of different instabilities. Coaxial atomization, in which a liquid jet is surrounded by an annular gas jet, is one of the most convenient and widely used methods of spray generation. A complete study of this atomization process involves breakup of the liquid jet, followed by the subsequent breakup and dynamics of fluid parcels and drops in turbulence, and with finally dispersion of fine droplets, potentially coupled with heat and mass transfer [7]. Many investigations have focused on the near-injector physics of the liquid jet breakup [8–12]. However, investigations in the far-field dispersed droplet region are scarce.

Nathana Machicoane ël (✉)
Univ. Grenoble Alpes, CNRS, Grenoble INP, LEGI, 38000 Grenoble, France
E-mail: nathanael.machicoane@univ-grenoble-alpes.fr

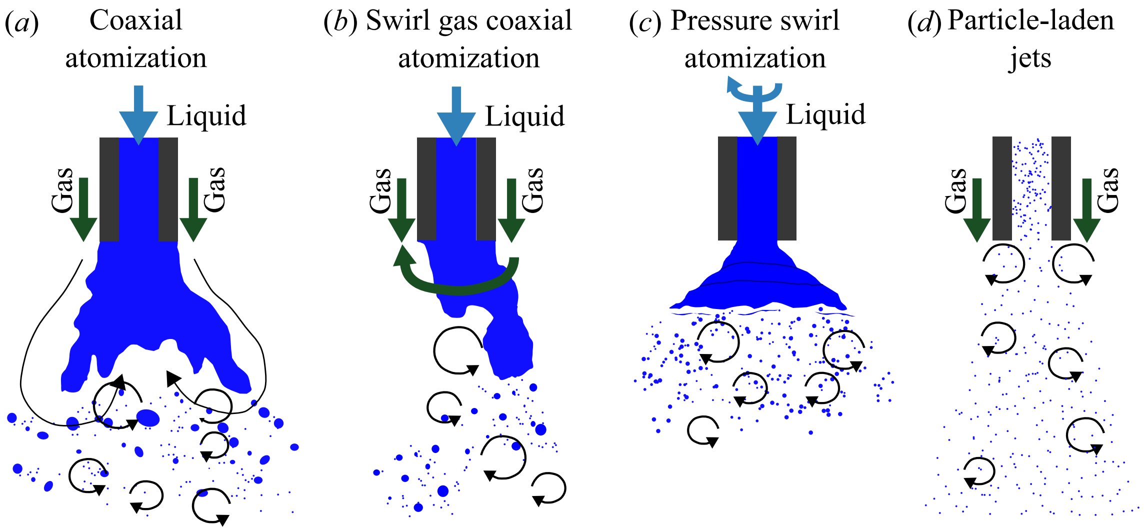

Fig. 1 Illustrative examples of spray formation from coaxial two-fluid atomization without (**a**) and with gas swirl (**b**), and from pressure swirl atomization (**c**), compared to a monodisperse particle-laden jet (**d**).

The investigation into the bulk liquid breakup to form a spray has been conducted in different dimensions. To list a few, past studies covered instability of bulk liquid [8,11], statistics and temporal dynamics of liquid jet breakup [13,14], droplet cluster behavior [15,16], dispersion of droplets [17–19], data science [20], interaction dynamics [21]. In addition to this, different effects are investigated, such as geometrical parameters [22], fluid and flow parameter [7,23], and some interaction of sprays with external forcing like electrostatics [24–26] or acoustics [27,28] have also been studied. On many occasions, the swirling motion of the droplets is desirable. While investigations on swirled liquid injection have been carried out for a long time, no tangential motion is imparted to the droplets after they breakup in such setups [29]. Therefore, in order to achieve some tangential motion for the droplets, swirling the gas jet is used to achieve tangential motion of the droplets. In addition, among the different methods of manipulating spray behavior, the introduction of swirl to the gas phase is known to change the breakup dynamics significantly [30,31]. However, the majority of the investigations are carried out very close to the nozzle, and findings related to swirling sprays are lacking.

As the gas jet has higher momentum in coaxial atomization, it has a substantial role in determining not only the breakup of the bulk liquid but also the droplet dispersion. The round gas jet from a nozzle has numerous important characteristics which many groups have identified over the years [32–35]. One of the significant features is the self-similarity behavior of the velocity components. Apart from the popular mean profiles, a few turbulence features are also known to be universal. For example, the Reynolds stresses, turbulence intensity [35], and integral length scales [36] are known to be self-similar quantities. Many of these features have also been reported for annular jet [37–39]. When high tangential motion of the gas jet is also present, a low pressure is created at the axis of the spray. This is known as vortex breakdown [40,41]. This can result in the enhanced spreading of the jet and alter the self-similar behavior of the jet. As a result, when a liquid jet is placed in such gas jets, the influence of these features on the resulting spray can be significant. However, investigations of the gas phase in a swirling spray have not received substantial attention, especially its turbulent characteristics.

Coaxial atomization involves a higher gas velocity than that of the liquid, leading to shear instability [11]. As a result, the Kelvin-Helmholtz type waves are formed on the interface of the jet. When the gas Weber number is small, these instabilities lead to alternating low-pressure and high-pressure regions, resulting in the meandering of the liquid jet, called flapping [7,10]. Consequently, the turbulence characteristics in the gas jet formed around the liquid jet play an important role in determining the trajectory of the droplets, with high prominence of large droplets at the edge [18]. With an increase in the Weber number, the length of the liquid jet decreases [42], reducing the meandering amplitude. Eventually, the dominant mechanism is Rayleigh-Taylor type instability, resulting in strips of liquid coming out of the jet [43]. This regime of breakup is called fiber-type atomization [7]. Due to high gas velocity in these conditions, entrainment plays a significant role. In addition, as the droplets formed are very small due to high stresses, one can expect that their behavior is close to that of the gas jet. When swirl is added to the gas jet, similar instabilities are reported; however, the flapping amplitude is known to be higher compared to the non-swirling condition [31]. As a result, the swirling spray can be understood to be wider than the non-swirling one.

Spray dispersion from coaxial atomizers, where inertial droplets are transported by the turbulent gas jet , involves physics that are studied in detail in particle-laden turbulence and particle-laden jets in particular [44] (Fig. 1d). Such investigations have required various experimental methods for deciphering different aspects of the flow [45]. The response of a particle to the continuous phase is often characterized by the ratio of particle response timescale (τ_p) to the flow timescale (τ_f), known as the Stokes number $St = \tau_p/\tau_f$. The interaction dynamics between a continuous phase and a discrete phase are essentially dictated by three factors. These are: (i) volume fraction of particles, (ii) particle to fluid density ratio, and (iii) particle size compared to the smallest turbulence scales [46]. While the first two factors are frequently considered in studies due to convenience, the third factor requires an in-depth analysis of the turbulent characteristics. The existing studies have a closer resemblance to particle-laden jets where monodisperse particles are used [47]. The results of these investigations primarily focus on how the particles respond to the continuous phase, the way they cluster, and how the turbulence in the gas phase is altered, among other features [44]. However, the majority of these studies focus on non-swirling jets [48].

The applicability of the results of particle-laden jets on sprays is limited due to the polydisperse nature of the droplets (as shown in Fig. 1), significant change in the concentration of droplets, both radially and as they travel downstream due to entrainment, and relatively very high gas velocity compared to most studies on particle-laden jets. Although few assessments have been conducted on clustering, droplet response, and mass flux [16,18,19,49], numerous questions fundamental to the understanding of sprays, specifically in the presence of swirl, are yet to be addressed. Little is currently known on the scaling of quantities relating to turbulent dispersion of large droplet in swirled flow, such as their velocity fluctuations and covariance. The present paper aims to answer such questions for a better understanding of the turbulent characteristics in swirling sprays.

2 Experimental method

A coaxial atomizer with central liquid jet (with diameter $d_l = 1.89$ mm and corresponding area $A_l = \pi d_l^2/4$) surrounded by annular gas (with inner and outer diameter $D_l = 3.1$ mm and $d_g = 9.985$ mm (with measurement accuracy of 1μm) and corresponding area $A_g = \pi(d_g^2 - D_l^2)/4$) is used in the present experiments (shown in Fig. 2a). Note that the quantities for liquid and gas are denoted by subscripts l and g, respectively. The interaction of the liquid jet with the gas jet occurs close to the nozzle and leads to the formation of a spray. Therefore, the fully developed liquid jet and the annular gas jet are controlled to provide a volume flow rate Q_l and Q_g, respectively. Corresponding exit velocity for the liquid jet is $U_l = Q_l/A_l$ and the Reynolds number is $Re_l = U_l d_l/\nu_l$, where ν is the kinematic viscosity. In the same manner, the gas jet velocity $U_g = Q_g/A_g$, Reynolds number $Re_g = U_g\sqrt{4A_g/\pi}/\nu_g$, and Weber number $We_g = \rho_g U_g^2 d_l/\sigma$ are calculated, where ρ is the density and σ is the surface tension of the liquid–gas interface. The non-dimensional parameters defined by combining both the liquid and the gas fluid and flow properties are the gas-to-liquid dynamic pressure ratio $M = \rho_g U_g^2/\rho_l U_l^2$ and liquid mass loading $m = \rho_l A_l U_l/\rho_g A_g U_g$, which are known to influence different behaviors in the spray formation process.

In the present experiments, the emphasis is on the influence of gas swirl on the spray. With a view to achieving this objective, the gas jet inlet to the atomizer is undertaken through two different sets of entries as shown in Fig. 2b. One set of inlets with Q_{NS} as the volume flow rate of gas entering coincident to the atomizer axis provides axial motion to the gas jet. Another set with Q_{SW} as volume flow rate is positioned off-axis to the atomizer axis, which provides tangential motion to the gas jet. Together they contribute to the total volume flow rate of gas entering the atomizer, i.e., $Q_g = Q_{NS} + Q_{SW}$. Such an arrangement leads to the Swirl Ratio $SR = Q_{SW}/Q_{NS}$. The values for the parameters used for the experiments are given in Table 1.

Distilled water as a liquid and filtered compressed air as a gas are used in the present experiments. For these fluids, the properties considered here are with respect to the room temperature of 20°C with a variation of up to 1.5°C. They are provided to the atomizer through an established spray generation setup, which has been well-characterized for the conditions under investigation in the present study [14,50]. The flow rate measurements are captured in real time along with the droplet properties. The variation of the flow rate with respect to the set value conducted *a posteriori* was observed to be less than 2%. For extracting the properties of the droplets produced from the setup, a 3-component phase Doppler particle analyzer (PDPA) was used as shown in Fig. 2c. The properties of the droplets of the spray are measured at different radial locations from

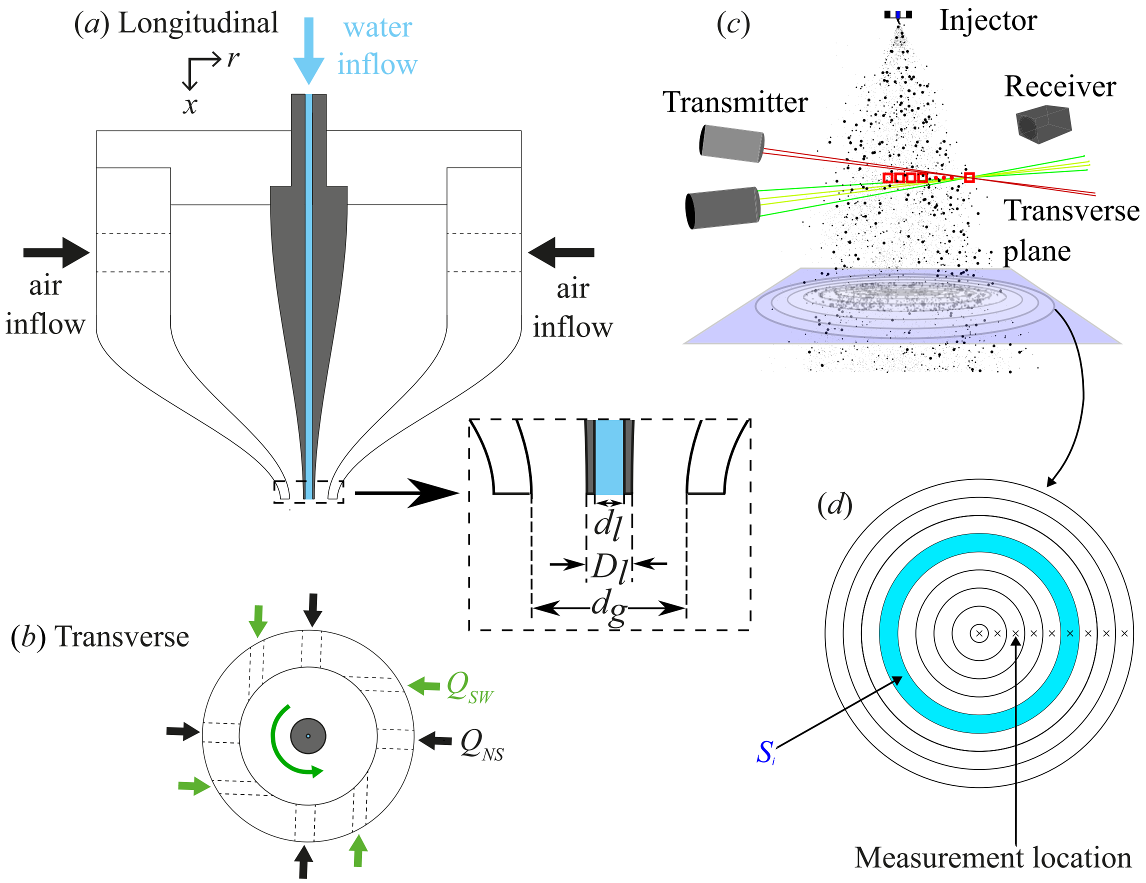

Fig. 2 Spray generation configuration and measurement technique. Coaxial atomizer used in the present experiments in a longitudinal cut (**a**), and (**b**) a cross-section in the plane of the gas inlets. The central dashed box is a zoomed-in view at the nozzle exit in the longitudinal cut of (**a**). (**c**) 3-component Phase Doppler particle analyzer arrangement and measurement locations in a spray longitudinal view and (**d**) cross-sectional, with anuli of area S_i representing each measurement location i

Table 1 The table of conditions with liquid Reynolds number $Re_l = \frac{U_l d_l}{\nu_l}$, gas Reynolds number $Re_g = \frac{U_g \sqrt{4A_g/\pi}}{\nu_g}$ and Weber number $We_g = \frac{\rho_g U_g^2 d_l}{\sigma}$, gas-to-liquid dynamic pressure ratio $M = \frac{\rho_g U_g^2}{\rho_l U_l^2}$, liquid mass loading $m = \frac{\rho_l A_l U_l}{\rho_g A_g U_g}$ and Swirl Ratio $SR = \frac{Q_{SW}}{Q_{NS}}$. The axial location where measurements take place is $x/d_g = 25$ for all conditions. In addition, for case 3 with $SR = 0$ and 0.8, the spray is investigated at $x/d_g = 10$ and 50

Case	U_l (m/s)	Re_l	U_g (m/s)	Re_g	We_g	M	m	SR
1	0.6	1120	82	52000	210	23	0.24	0, 0.8
2	0.6	1120	115	72700	420	46	0.17	0, 0.8
3	0.6	1120	163	102400	830	90	0.12	0:0.2:1
4	0.6	1120	203	127700	1280	140	0.1	0, 0.8
5	1.2	2230	163	102400	830	23	0.24	0, 0.8
6	2.3	4350	163	102400	830	6	0.47	0, 0.8
7	4.5	8480	163	102400	830	2	0.91	0, 0.8

the center of the spray to the edge for a particular axial location, as shown in Fig. 2d. In each location, data was collected for 25 min or 500000 droplets, whichever was reached earlier.

The PDPA essentially consists of transmitters that focus laser beams to form a probe volume and a receiver that collects the light scattered by droplet crossing the probe volume. Each of them has lenses for the appropriate modification of the laser beams and scattering signal. In the present experiments, we used a collimating lens on the transmitter and an imaging lens on the receiver with focal lengths $f_c = f_i = 500$ mm, resulting in a magnification $\beta = -f_i/f_c$. For the measurement of each component of velocity, a pair of laser beams is required. Lasers corresponding to the axial U and radial V components (refer Fig. 2) intersect to make a prolate spheroid. A laser pair for the tangential velocity component W is incident on the other two pairs at the location of their intersection at angle of 30°. The PDPA was operated in a forward scattering mode with the scattering angle of 49°. The probe volume formed by the intersection of the laser beams is trimmed with the aid of a spatial filter in the receiver with slit width $s = 200\ \mu$m. This combination of optics produced a cylindrical probe volume of effective length $s/|\beta| sin\theta$. As this equipment was operated in coincident mode, the data obtained on each drop consisted of simultaneous measurement of its diameter d, axial, radial, and tangential velocities. Note that PDPA can only measure a single spherical drop at each moment. For this purpose, each droplet was phase validated to ascertain the quality of data collected.

The PDPA was set to measure drops in the range $1-100\ \mu$m. As the attention of this work is on deciphering the gas phase accurately without compromising significantly on the majority of the drops, such an arrangement was preferred. For identification of the gas phase in the presence of spray, small droplets with $d < 5\ \mu$m are considered. The size was ascertained by finding the Stokes number at the exit of the nozzle, given by:

$$St_d = \frac{\tau_p}{d_g/U_g}, \tag{1}$$

where $\tau_p = \rho_\ell d^2/\left(18\rho_g v_g\right)$ is the time scale for response of droplet size d. For droplets of 5 μm, the maximum exit Stokes number value obtained for any condition in the present investigation was 0.002. This is less than the critical value of 0.01 proposed in the literature to consider particles as tracers [44]. Since the Stokes number decreases with the axial distance, droplets below 5 μm can be conservatively assumed to be tracers. In addition, to determine the characteristics of the non-swirling gas phase in the absence of the spray, a hotwire anemometer was used at a sampling rate of 20 kHz for 10 s at different locations.

3 Velocity statistics

The following nomenclature is used in this article: The exit jet velocity is U_J. The instantaneous velocity component in the axial direction is U, in the radial direction is V, and in the tangential direction is W. Quantities within $\langle . \rangle$ represent the mean values, small alphabets indicate the centered variables for the same quantities, and an apostrophe represents the standard deviation. For example, the total axial velocity U is decomposed as $U = \langle U \rangle + u$, with an average $\langle U \rangle$ and standard deviation u'.

Different components of droplet velocity in a spray span over different ranges, leading to fluctuations in the spray. Figure 3 demonstrates two representative cases of sprays. In both of these conditions, the spatially nonuniform droplet concentration is evident. This behavior can be understood to be not only a consequence of turbulence but also a contributor to the velocity fluctuations. To realize these variations quantitatively, it is essential to begin the investigation by looking into the detailed statistics of the velocity components.

3.1 Local droplet velocity distributions

The probability density functions of different velocity components of the droplets for a low We_g condition, when the liquid jet flaps substantially, are presented in Fig. 4a. These distributions are obtained for different radial locations: center, edge, and a region between these two locations. Different droplets of different sizes contribute to these distributions, but note that smaller droplets are more abundant in the spray [49,51]. Focusing on the axial velocity for non-swirling and swirling sprays, it is easily noticeable that the velocity ranges are different at different locations and also with the presence or absence of swirl. While the droplet axial velocity away from the edge has a rounded shape, at the edge, the distributions are peaked, with a seemingly exponential tail and a pronounced maximum around 0 m/s, which indicates their relatively insignificant deviation from the mean compared to other locations. In addition, the axial velocity for the non-swirling condition is observed to be more positively or negatively skewed compared to its swirling counterpart, indicating that swirl imparts more isotropicity to the axial behavior of the spray at the center. In the same essence, one can observe a positive skewness (and note that the other side would be negatively skewed) for the axial velocity in the mid-region and the edge compared to the center for both non-swirling and swirling conditions.

The droplet mean radial velocity in a spray is typically one order of magnitude smaller than the axial velocity. However, from the second column of Fig. 4a, at the edges, both velocities can be observed to be of the

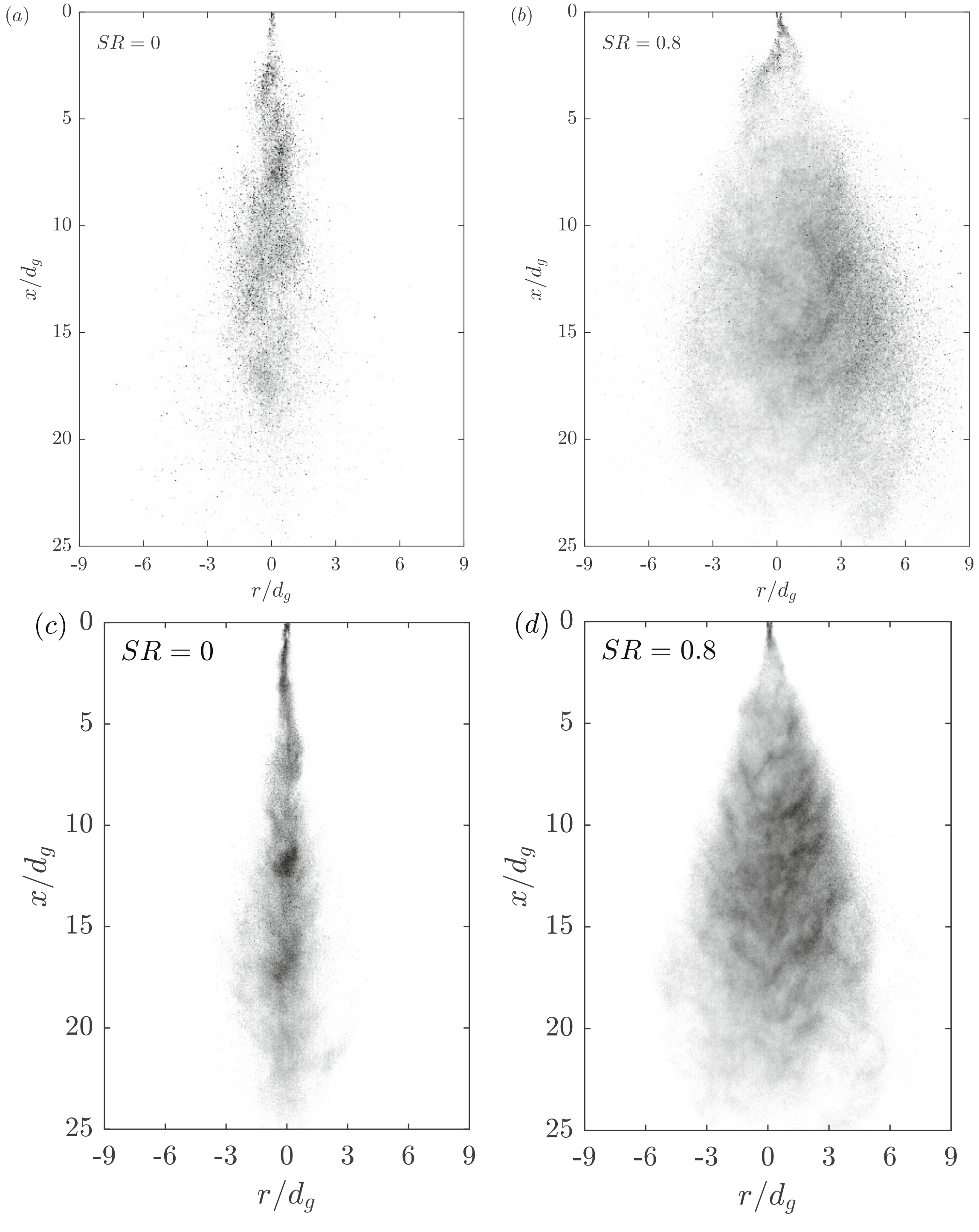

Fig. 3 Scattering images of droplet generation and spray dispersion at $SR = 0$ (**a**, **c**) and $SR = 0.8$ (**b**, **d**) for $Re_l = 1120$ and (**a**,**b**) $We_g = 210$, (**c**,**d**) $We_g = 830$

same order of magnitude. Except at the edge, V becomes more symmetric about its mean with the introduction of swirl in the gas jet. It is also important to notice that swirl also leads to tighter distributions of the radial velocity. A similar observation can also be observed in the case of tangential velocity W.

At higher Weber numbers (Fig. 4b), the droplet axial velocity distributions are observed to be symmetric about their mean in the center and the edge in the absence as well as presence of gas swirl, while retaining

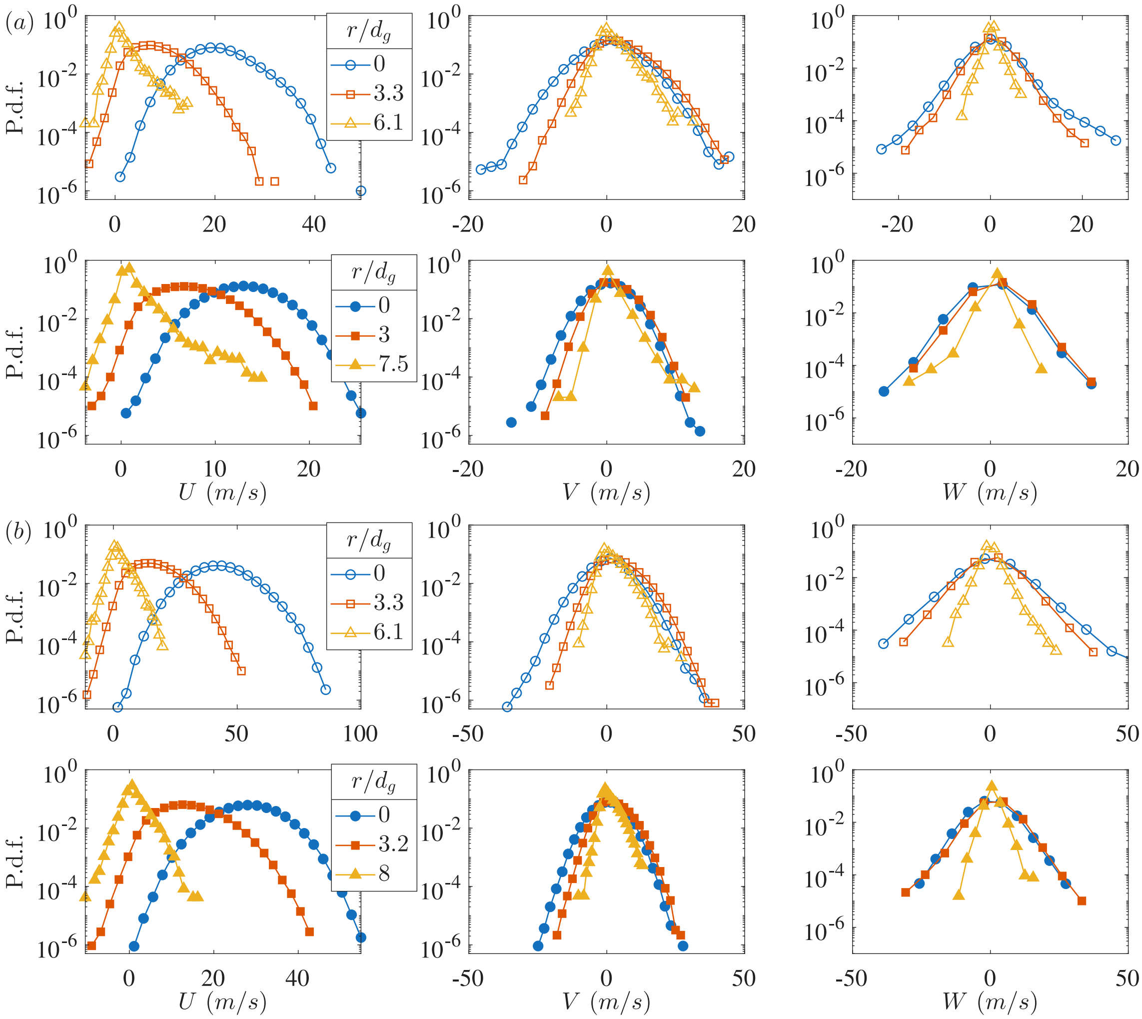

Fig. 4 Local probability density functions of velocity components at several radial distances r for $Re_l = 1120$, $We_g = 210$ (**a**), and $We_g = 830$ (**b**). In each subfigure, Top row : $SR = 0$ Bottom row: $SR = 0.8$

a similar skewed behavior for the mid-region as in the case of low We_g. Such distributions indicate a higher degree of isotropicity for high gas Weber number sprays. In addition, V and W are observed to have a similar influence on the swirl. Based on the distribution of these two velocities for both the We_g one can infer that swirl leads to tighter distributions overall, which will be investigated locally below through the velocity standard deviations.

We remind the reader here that these statistics are based on a single axial location along the radius of the spray. However, its contribution to the whole spray depends on the annular area it represents in the spray plane (Fig. 2d). Therefore, it is imperative to investigate the global droplet velocity behavior and how they are influenced by swirl.

3.2 Distribution of global velocity fluctuations

The global probability distribution of the fluctuating velocity of droplets is calculated by

$$p_i = \frac{\sum_j N_{ij} S_j / T_j}{\sum_i \sum_j N_{ij} S_j / T_j}, \tag{2}$$

where N_{ij} is the number of particles in class i of the centered velocity (for example, for axial velocity, we calculate the $U - \langle U \rangle$ and divide it into N bins) at location j, S_j is the area which the location j represents

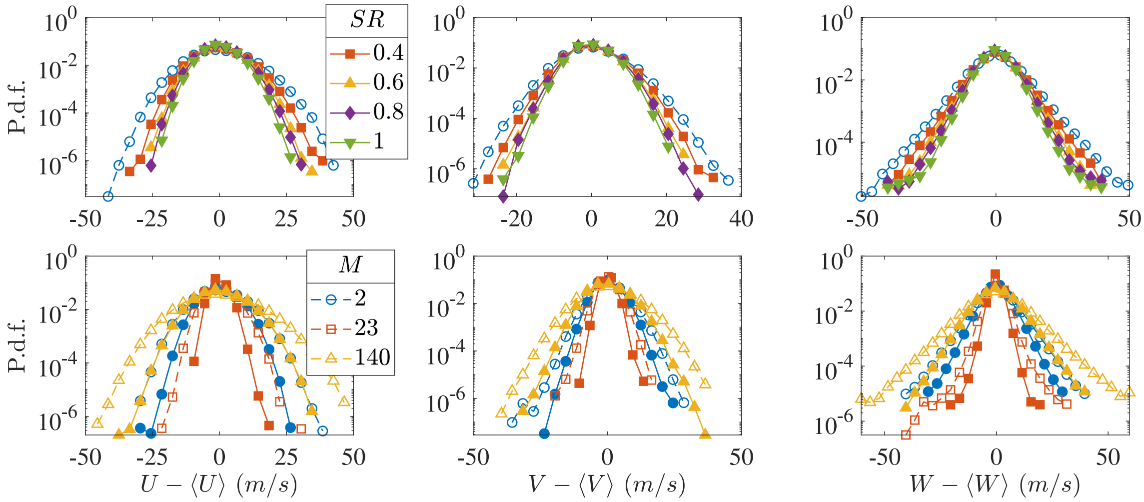

Fig. 5 Global probability density functions of velocity components at $x/d_g = 25$ for various conditions. In the first row $Re_l = 1120$ and $We_g = 830$, and the second row uses cases 1, 4 and 7 from Table 1. The closed symbols are for non-swirling spray and the open ones are for swirling conditions. Closed symbols in the second row are for $SR = 0.8$

(Figure 2(d)). The probability density functions derived from this formula are shown in Fig. 5 for different swirl ratios SR (top row) and different gas-to-liquid dynamic pressure ratios M (bottom row).

It is well-known that the axial velocity of droplets decreases with the increase in SR, especially when the influence of swirl becomes prominent [19,49]. With this aspect in mind, we observe that the span of the distributions of u decreases as swirl increases, which indicates that swirl leads to decreased turbulence level from the axial component of velocity. Focusing on the first plot in the second row, the mentioned observation can be further corroborated across varying M, We_g, and Re_l.

Figure 5 second and third columns demonstrate the global probability distribution of the fluctuating velocities corresponding to the radial (V) and the tangential (W) components. In the same manner as for U, both of these components also have a lower range of fluctuations with increased SR, irrespective of M. The cumulative understanding from these plots is that with an increase in the swirl, the spray's global behavior is more often aligned with its mean quantities. These analyses logically point to the direction of quantification of the velocity fluctuations.

3.3 Average velocity and turbulence intensity at the spray axis

Before proceeding to the turbulence characteristics, we show the mean centerline velocity variation of the gas phase non-dimensionalized with its exit gas velocity in Fig. 6a. We remind the reader here that in the absence of spray, the gas jet is measured by a hotwire anemometer, while in the presence of spray, it is measured by identifying the small droplets (i.e., $d < 5\ \mu$m) from the PDPA measurements. It is observed that this axial velocity decreases with an increase in SR. The variation follows observations made on the axial velocity distributions U of Fig. 4b. In addition, it is important to note that the influence of swirl is prominent only for $SR \geq 0.4$. Similar observations have been reported earlier as well [52,53].

Figure 6(b) presents the centerline fluctuation of gas jet at varying axial locations in the absence and presence of spray. Primarily three features can be inferred from these plots: (1) the presence of spray modifies the development of turbulence in the turbulent jet, starting more upstream but reaching a smaller value than without spray (i.e., higher turbulence intensity at low values of x/d_g and lower turbulent intensity at higher x/d_g), (2) the values tend to saturate as the measurements are conducted far from the nozzle in the absence or presence of spray (also observed for round gas jet with similar saturation value [34]), and (3) swirl does not tend to affect the turbulent intensity of the spray beyond certain axial distance.

The gas jet close to the nozzle interacts with the liquid jet in various ways depending on the regime of breakup. Specifically, the condition in Fig. 6 results in fiber-type atomization, where the liquid jet is quickly truncated and acts like a backward-facing step for the gas outlet flow [18]. As a result, the interactions between the gas and liquid phase at the exit of the jet promotes fluctuations (due to the wakes of the liquid

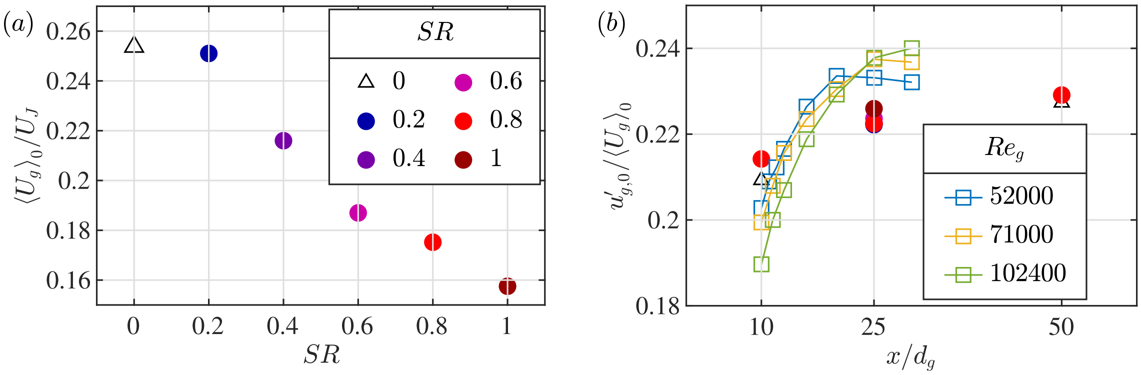

Fig. 6 Centerline gas jet behavior for various locations and swirl ratios. **(a)** Variation of mean centerline axial velocity ($\langle U_g \rangle_0$) of the gas jet normalized by the exit velocity with the change in SR at $x/d_g = 25$, and **(b)** Variation of centerline turbulent intensity with an increase in axial distance from the nozzle. The symbols without any line correspond to a spray conditions when $Re_g = 102400$ and $Re_l = 1120$, with open symbols for $SR = 0$ and closed symbols for $SR \neq 0$. Open symbols with line are from hotwire measurements in the absence of spray

structures, that are ever changing, such as the wake behind a flag, while when there is no liquid, a steady recirculation is expected, and no such shedding/multifrequencies), and hence, an increase in turbulence is expected. Consequently, feature (1) occurs. However, the change in behavior at high axial distance is a result of attenuation in turbulence of the gas phase due to the presence of inertial droplets that damp some turbulence. Such attenuation in turbulence occurs when the volume fraction of particles (α) in dispersed gas is in between 10^{-6} and 10^{-3}, and the Stokes number $St < 1$ [54]. The spray resembles a particle-laden jet when it is far away from the nozzle, and therefore, feature (1) is thoroughly justified. However, far downstream of the nozzle, substantial entrainment and spread of the jet result in the decrease of volume fraction α. Consequently, the turbulence in the continuous phase does not get affected far away from the nozzle. Hence, feature (2) is observed.

3.4 Radial profiles of the velocity fluctuations

Following the discussion on turbulence intensity at the center of the spray, an investigation into the turbulence at different radial locations is desirable. To understand various aspects of turbulence in sprays, we segregate the investigation for different components of velocity into two parts. One part corresponds to the gas phase, i.e., when the droplets are less than 5 μm, leading to tracer-like behavior ($St < 0.002$, [49]), and the other part corresponds to the big droplets, i.e., when the drop size is larger than 10 μm.

Figure 7(a,b) demonstrate the radial profiles of gas phase axial fluctuations non-dimensionalized with the centerline axial velocity. The mean axial velocity half-width $r_{0.5}$ is the radius at which $\langle U_g \rangle = 0.5 \langle U_g \rangle_0$ at the same spray plane. The fluctuation profiles overlap with varying SR. However, a slight deviation occurs toward the edge of the spray, and the value increases with an increase in SR. On the other hand, for low M conditions, the superimposition of non-swirling and swirling cases of non-dimensional fluctuation does not occur even on the centerline. In contrast, the big droplets are observed to be more sensitive to SR at the center (Fig. 7c and d). Note that for $M = 23$ (Fig. 7d), there is flapping instability in the liquid jet, leading to excursion of large droplets. In addition, due to the high Re_l value at $M = 2$, the long liquid jet meanders, presenting successive crests and troughs. Understandably, these occurrences lead to highly turbulent behavior at the edge of the spray, especially in the presence of swirl. Therefore, at the edge, fluctuations are high for these conditions. Note that for low-swirling conditions at high M, the maxima of the droplets' axial fluctuations are at the center. Otherwise, i.e., when the swirl is high and/or M is low, an off-centered maxima in the fluctuation profile is encountered. Therefore, the noticeable influence of swirl is to make the big droplets fluctuate with a more similar level to the gas phase, especially at the spray center.

Performing a similar investigation of the fluctuation of the radial velocity of the gas phase, we observed that unlike the case of axial velocity fluctuations and well-known self-similarity behavior in mean flows in $\langle U \rangle$ and $\langle V \rangle$, there is no collapse of the radial profiles of radial velocity fluctuations over variations of M and SR. In fact, it makes the understanding more difficult as the swirl leads to different centerline velocities and hence comparison of fluctuations is due to two phenomena being represented simultaneously. Therefore, Fig.

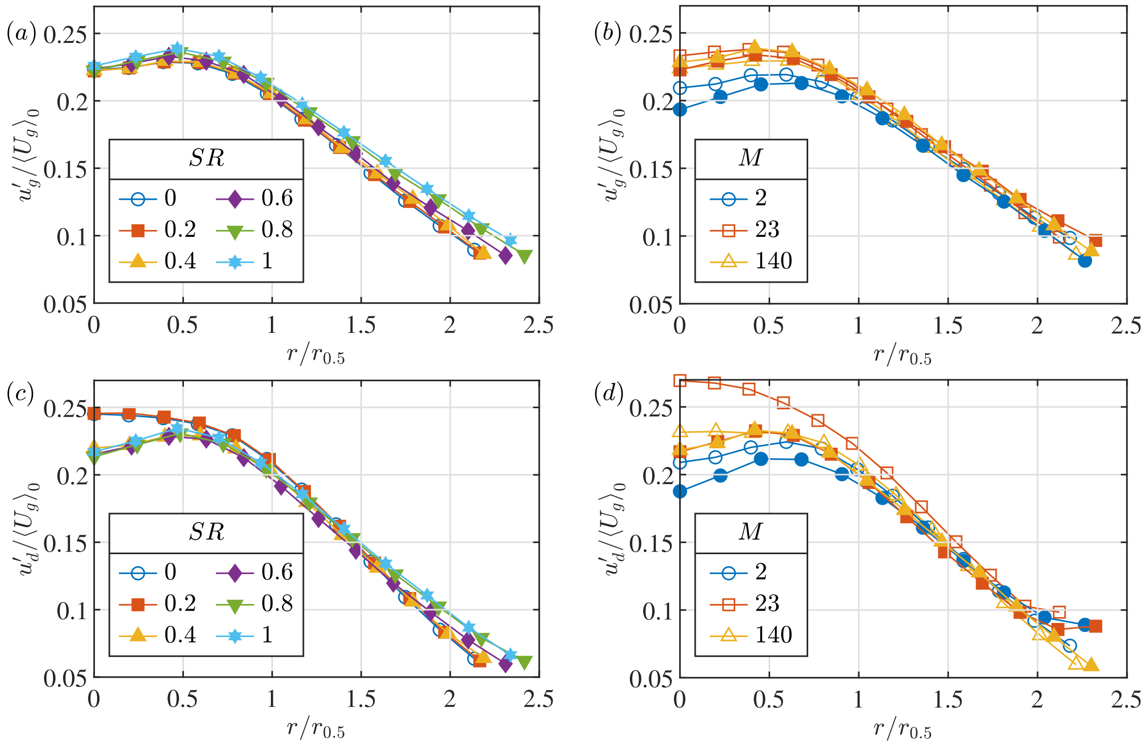

Fig. 7 Radial profiles of the axial velocity fluctuations for gas phase (**a**, **b**) and droplets larger than 10 μm (**c**, **d**), measured at $x/d_g = 25$, and normalized with their mean gas centerline axial velocity shown as a function of radius non-dimensionalized with the gas velocity half-widths. The non-swirling conditions are shown with open markers and swirling conditions are shown with filled markers. Note that $\langle U_g\rangle_0$, $\langle U_d\rangle_0$ and $r_{0.5}$ depend on the operating condition (including variation of swirl ratio). (a, c) For all SR values at $Re_l = 1120$ and $We_g = 830$, and (b, d) non-swirling and swirling conditions for three M values (cases 1, 4 and 7)

8(a,b) show the radial fluctuations normalized by the exit jet velocity U_J. It is straightforward to observe that swirl reduces the radial fluctuations. This result is in accordance with the observation in Fig. 5. However, the droplet radial velocity fluctuations are observed to be maximum away from the center of the spray (Fig. 8c) when the effect of swirl is not substantial, in contrast to the radial profile of axial velocity fluctuation. Figure 8(d) further reveals that this behavior persists for all M values. A similar observation can be drawn for the tangential velocity component w', which is not shown here for conciseness.

Figure 9 highlights the level of turbulent fluctuation in the gas phase and the droplet phase, using the non-dimensionalized velocity fluctuation norm $\sqrt{u'^2 + v'^2 + w'^2}$. We observe that swirl reduces the level of fluctuation in the spray significantly when the effect of swirl is meaningful. In addition, we observe that the profiles' maxima are off-center, due to the substantial contribution of the axial velocity component. However, the magnitude of the maxima reduces due to the varying effect of the fluctuations from the other two components of velocity. The gas phase fluctuation amplitude is observed to be more than that of the droplet phase. This observation indicates the inertia effect on the big drops. As a result, these droplets are less prone to being affected by turbulent fluctuations in the medium.

4 Reynolds stress, fluctuating velocity, covariance, and turbulence phenomenology

A deeper understanding of the spray behavior following the investigation of the first and second-order statistics comes from the analysis of the velocity covariance, where one velocity component is related to another velocity component. Similarly, the covariance will be discussed for the gas jet, in which case it corresponds to the Reynolds stress terms, and for the big droplets, where it informs on their transport properties.

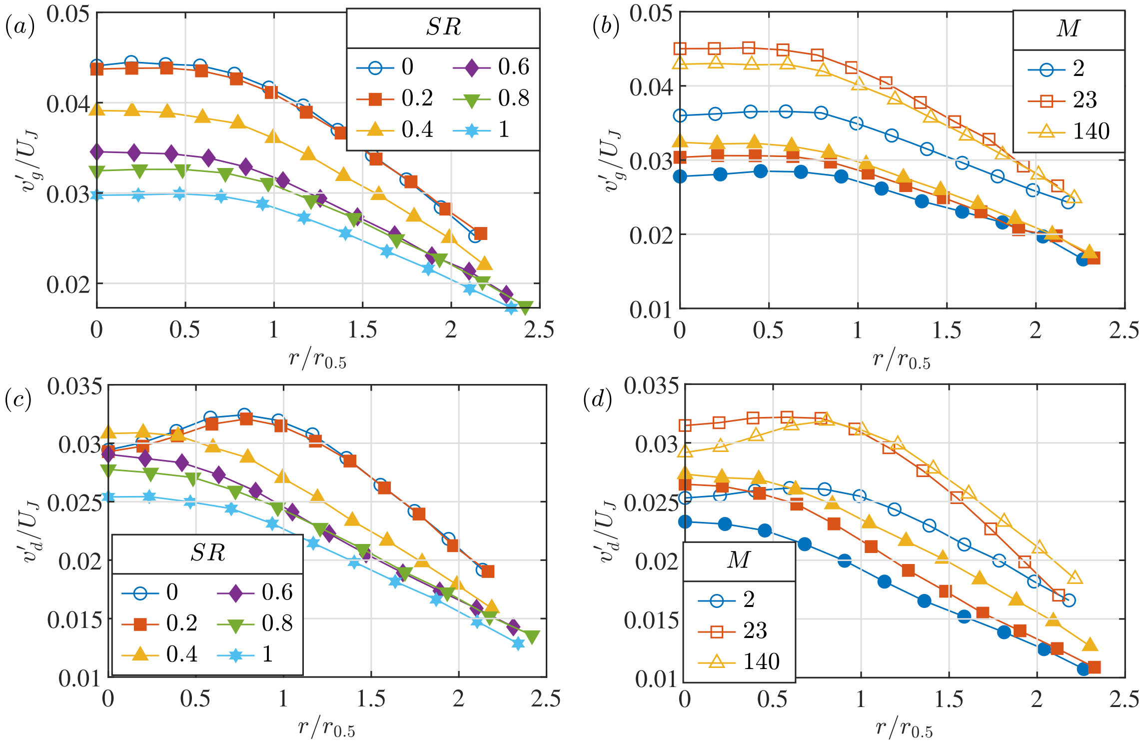

Fig. 8 Radial profiles of the radial velocity fluctuations for gas phase (**a**, **b**) and droplets larger than 10 μm (**c**, **d**) - note the change in axes - measured at $x/d_g = 25$, and normalized with the exit gas jet velocity shown as a function of radius non-dimensionalized with their gas velocity half-widths. The non-swirling conditions are shown with open markers and swirling conditions are shown with filled markers. (a, c) For all SR at $Re_l = 1120$ and $We_g = 830$, and (b, d) non-swirling and swirling conditions for three M values (cases 1, 4 and 7)

4.1 Gas Reynolds stresses and particle fluctuating velocity covariance

Figure 10(a,b) demonstrate the Reynolds stresses corresponding to the axial and the radial components of velocity fluctuations $\langle uv \rangle$ for the gas phase using the small droplets (< 5 μm) from the PDPA measurements. It is observed that there is a proper collapse of these profiles for sprays with different swirling intensity (Fig. 10a). This collapse between swirling and non-swirling conditions can also be observed at different M values (Fig. 10b). The self-similarity of this Reynolds stress term is well-established in the literature [35,55]. Therefore, the trends for the gas phase here indicate that there is a self-similarity behavior of the Reynolds stresses for the gas even in the presence of spray, for both swirling and non-swirling conditions. A physical interpretation for this behavior is that axial and radial fluctuating velocities for the gas phase are correlated to the same extent at a given non-dimensional radial location, irrespective of conditions.

The radial profiles of the droplet fluctuating velocity covariance between the axial and radial components are shown in Fig. 10(c,d). There are clear distinctions from the behavior of the gas phase (Fig. 10a,b). The self-similarity observed for the gas phase does not exist for the big droplets. In addition, the magnitude of the covariance is observed to increase with the swirl ratio (Fig. 10(c). It is also interesting to note that the maxima of this correlation move toward the spray axis with an increase in the swirl ratio. Focusing on these aspects for conditions with different M, one can realize that at high Re_l, $\langle u_d v_d \rangle$ deviates from the profiles found at higher M. One can therefore deduce that for big droplets, the relation between fluctuations of axial and radial components is condition-dependent, and therefore, has variable fluctuating behavior. The observation of shifting maxima toward the spray axis for the swirled condition compared to the no-swirl conditions found for the gas Reynolds stress is also made here.

The literature for non-swirling round jets mentions that the Reynolds stress component $\langle vw \rangle$ is zero due to circumferential symmetry [32]. This is not the case here, as even the non-swirling gas jet is prone to instabilities that excites non-axisymmetric modes such as helical modes, beyond possible additional symmetry breaking caused by the presence of the spray. For a better understanding of this aspect in swirling sprays, we show these

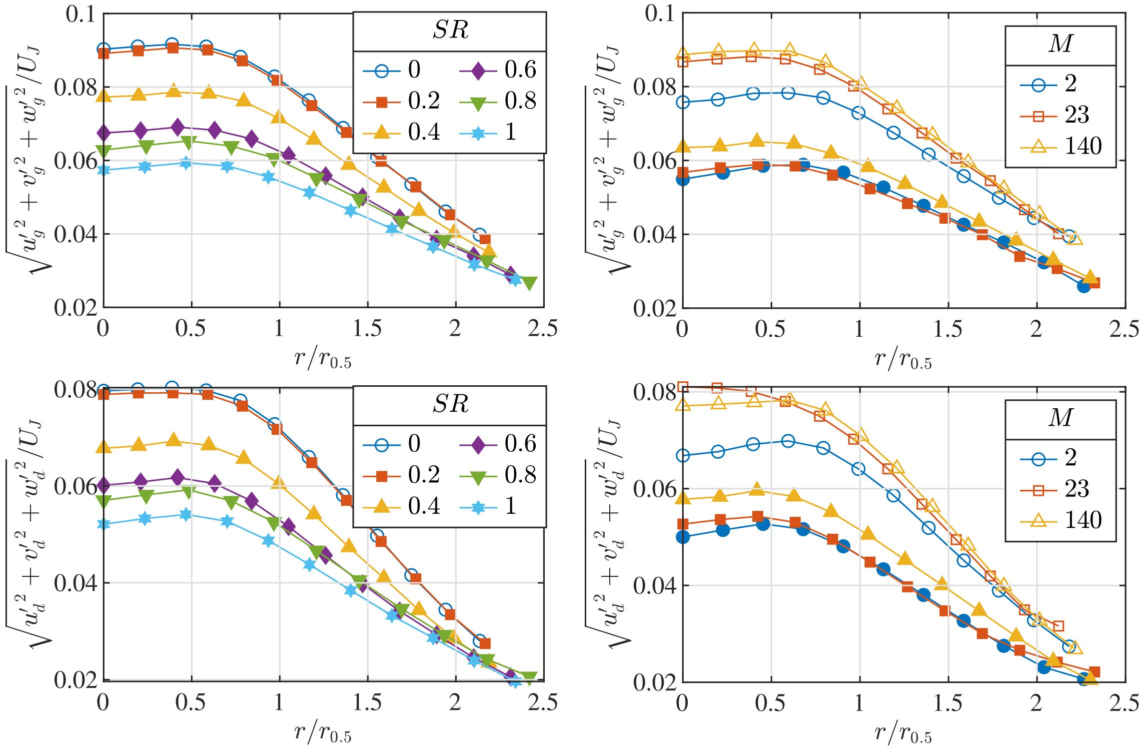

Fig. 9 Radial profiles of the velocity fluctuation norm for gas phase (**a**, **b**) and droplets larger than 10 μm (**c**, **d**), non-dimensionalized by the exit gas velocity, shown as a function of radius non-dimensionalized with their gas velocity half-widths. The measurements are conducted at $x/d_g = 25$. The non-swirling conditions are shown with open markers and swirling conditions are shown with filled markers. (**a**, **c**) For all SR at $Re_l = 1120$ and $We_g = 830$, and (**b**, **d**) non-swirling and swirling conditions for three M values (cases 1, 4 and 7)

results for various conditions in Fig. 11 (a,b) for the gas phase in the presence of spray. We observe that $\langle vw \rangle$ decreases with an increase in the radial length, irrespective of SR and M, with no indication of self-similarity. Near the spray axis, $\langle v_g w_g \rangle$ is higher for low-swirling flows, as the high-swirl conditions display flatter profiles, with higher covariances values for $r/r_{0.5} > 0.5 - 1$ than their no-swirling counterparts. However, one can observe that for low M values, when there is a prominent swirl, the maxima of the stress component are away from the center. A look at these profiles for large droplets (> 10 μm) points to a few interesting features. There is an overall increase of $\langle v_d w_d \rangle$ with an increase in SR. In addition, while the values are one almost order of magnitude lower in comparison to the gas phase behavior, the radial profiles are flatter, i.e., the values are almost constant across the spray plane. It can also be noticed for large droplets that the covariance profiles are not flat for lower value of M, and display an off-centered maximum when $SR = 0.8$.

A similar investigation for the Reynolds stress component $\langle uw \rangle$ is shown in Fig. 12. We observe that for the gas phase, while the values are very small, there is a definite trend of initial increase followed by a decrease with increasing radius for any SR. There is also a similar crossover point between low-swirling conditions and the swirling ones as observed in Fig. 11a. These observations also hold true for different M values (Fig. 12b). Similarly, a look at the big droplets (> 10 μm) is observed to indicate similar trends (Fig. 12c, d). It should be noted that the values for $\langle uw \rangle$ are roughly 5 times small with respect to $\langle uv \rangle$, with similar order of magnitude for both the gas and the big droplets. However, similar to the previous component of Reynolds stress, the reason for a non-zero value throughout the plane perpendicular to the jet axis (contrary to literature [32]) is the breakdown of the axisymmetry of the jet due to presence of instabilities like the helical modes.

4.2 Spray turbulence analysis

While the Reynolds stress terms further characterize the spray turbulence behavior and can help modeling aspects for instance, the complexity associated with turbulent flows necessitates it to be characterized through

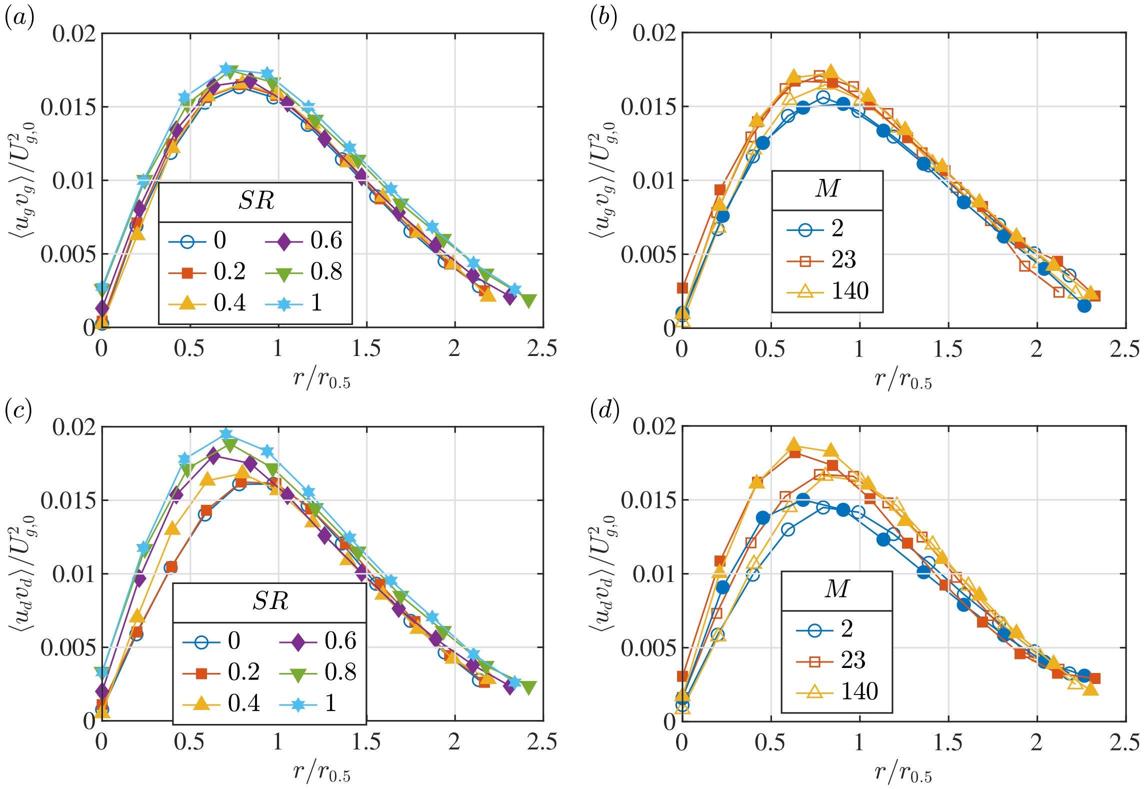

Fig. 10 Radial profiles of the covariance between the axial and radial fluctuating velocities for the gas phase (**a**, **b**) and droplets larger than 10 μm (**c**, **d**), measured at $x/d_g = 25$ and non-dimensionalized by the square of their centerline gas velocity, shown as a function of radius non-dimensionalized with their gas velocity half-widths. The non-swirling conditions are shown with open markers and swirling conditions are shown with filled markers. (**a**, **c**) For all SR at $Re_l = 1120$ and $We_g = 830$, and (**b**, **d**) non-swirling and swirling conditions for three M values (cases 1, 4 and 7)

additional quantities. Therefore, Fig. 13 illustrates a few of the spray turbulent characteristics through different parameters by identifying the gas dynamics from the small droplet measurements. The point-like nature of the measurements yield time series of velocity at each radial location, separated into the mean and fluctuating velocity components. The analysis rely on the axial fluctuating velocity auto-correlation function. The auto-correlation function $R_{uu} = \langle u(t)u(t+dt)/u^2 \rangle$ with respect to the time lag (dt) is shown in Fig. 13(a) for different radial locations for a high We_g condition without and with swirl. These curves display a shape resembling the exponential decay usually observed in turbulent flows. We observe that the correlation time, the timescale associated to how quickly the function decreases, increases with an increase in the radial distance and also with the introduction of swirl in the gas flow.

The turbulent integral time scale is defined as the integral of the velocity auto-correlation function, $T = \int_0^\infty R_{uu}(dt)d(dt)$. It corresponds to the local flow large scale, and can be used to compute other turbulent quantities. To alleviate biases caused by noise, the auto-correlation is integrated only up to the time lag at which the function reaches 0.05 to compute T. While implying a very small underestimation of T, the actual value of that threshold does not change the trends shown hereafter. The integral length scale is calculated based on the local mean velocity $U(r)$ and the integral time scale as $L = TU$. The turbulent dissipation rate is then calculated from the velocity fluctuation and the integral length scale as $\varepsilon = u'^3/L$. The radial profiles of the dissipation rate for various swirl ratios for a high Weber number condition are shown in Fig. 13(b). It is clearly inferred that the dissipation rate decreases with an increase in the radial length for all conditions as expected in a turbulent jet. Note that the ε decreases very steeply for the low-swirling conditions, which points to a thin mixing layer. In addition, a decrease in the dissipation rate is also observed with an increase in the swirl ratio, pointing to reduced turbulent energy as observed earlier. This decrease is around 75% from non-swirling to high-swirling conditions, suggesting a significant role of swirl in the dissipation rate of turbulent energy.

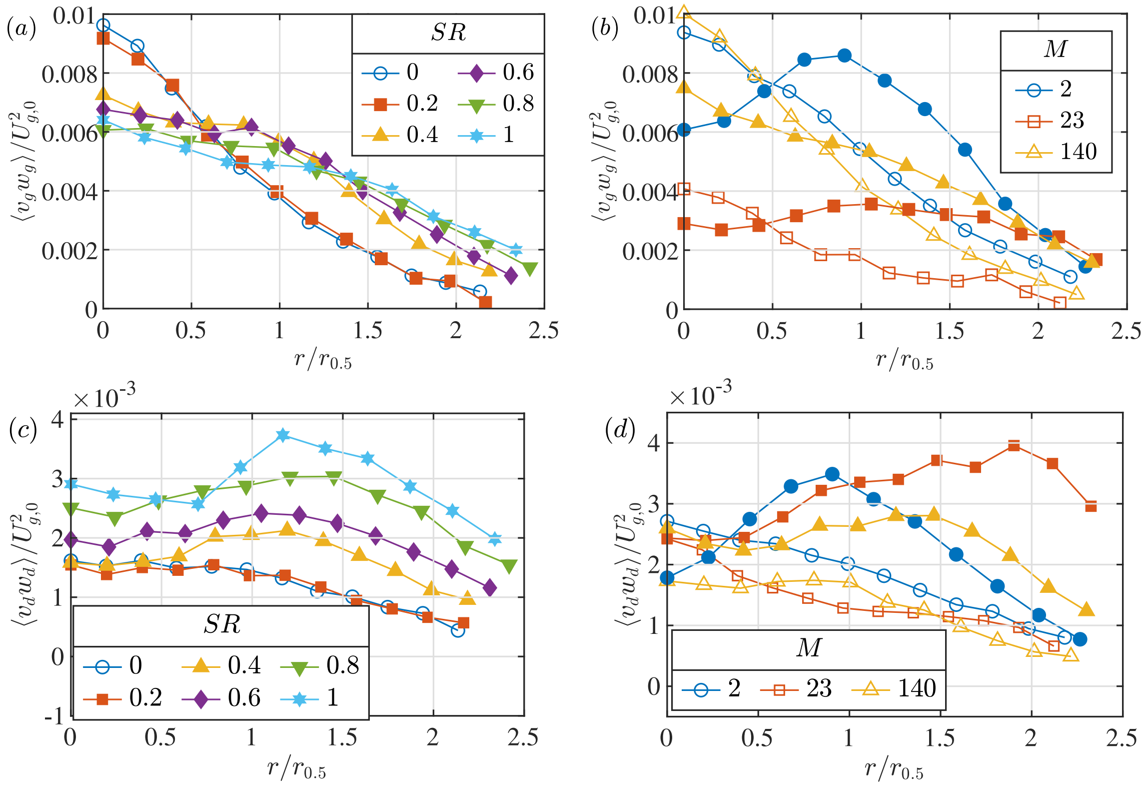

Fig. 11 Radial profiles of the covariance between the axial and radial fluctuating velocities for the gas phase (**a**, **b**) and droplets larger than 10 μm (**c**, **d**), measured at $x/d_g = 25$ and non-dimensionalized by the square of their centerline gas velocity, shown as a function of radius non-dimensionalized with their gas velocity half-widths. The non-swirling conditions are shown with open markers and swirling conditions are shown with filled markers. (**a**, **c**) For all SR at $Re_l = 1120$ and $We_g = 830$, and (**b**, **d**) non-swirling and swirling conditions for three M values (cases 1, 4 and 7)

A typical calculation of Stokes number in the sprays is based on on an estimation of the integral timescale through an inlet large-eddy turnover time simply defined as d_g/U_J [18]. This leads to an underestimation of the Stokes number compared to using the actual integral time already, which becomes a drastic underestimation compared to a definition based on the Kolmogorov time scale τ_η. This discrepancy grows for high Weber numbers sprays as the scale separation follows $T/\tau_\eta \sim \sqrt{Re_L}$, where $Re_L = u'L/\nu_g$ is the integral scale Reynolds number. Therefore, we calculate $\tau_\eta = (\nu/\varepsilon)^{0.5}$ and $\tau_d = \rho_\ell d^2 / \left(18\rho_g \nu_g\right)$ to compute the turbulent Stokes number $St_d = \tau_d/\tau_\eta$. Note that the Stokes number is computed locally and only the centerline values are shown here for conciseness, as they correspond to the maximum values of St_d. The variation of St_d with increase in droplet diameter at the centerline of the spray is shown in Fig. 13(c). While trivially showing $St_d \sim d^2$, this plot clearly identifies that the droplets of the order of 0.1 μm can only truly behave as fully faithful flow tracers, with Stokes number values below the threshold of 10^{-2} typically used in particle-laden turbulence [44]. However, droplets of the order of 1 μm, with Stokes number approximately unity, i.e., responding with time scales of the order of τ_η, can be considered here as partial tracers (which is further discussed in Sec. 5). This consideration is essential due to the feasibility of generating and measuring the size and velocity components of droplets of this size, rather than 0.1 μm, for any practical purpose. Note that due to such practical purposes, drops larger than 1 μm (up to even 10 μm) are typically used to infer the gas velocities in sprays. The present plot clearly showcases that such droplets are actually highly inertial and may lead to biases in estimating the carrier phase quantities.

Figure 13(d) aims to present a similar assessment with the change in gas Weber number We_g. We show the turbulent Stokes number for two different sizes of droplets, 5 and 10 μm. Non-swirling and swirling conditions are shown for each of the droplet sizes. Once again, it is trivial that doubling the drop size increases the Stokes number by 4 times, but it makes easy access to the actual magnitude, which for instance is reduced by roughly two when swirl is added to the gas jet. It can therefore be concisely mentioned that finer droplets become increasingly necessary as We_g increases. It must be noted here that finer droplets are produced from

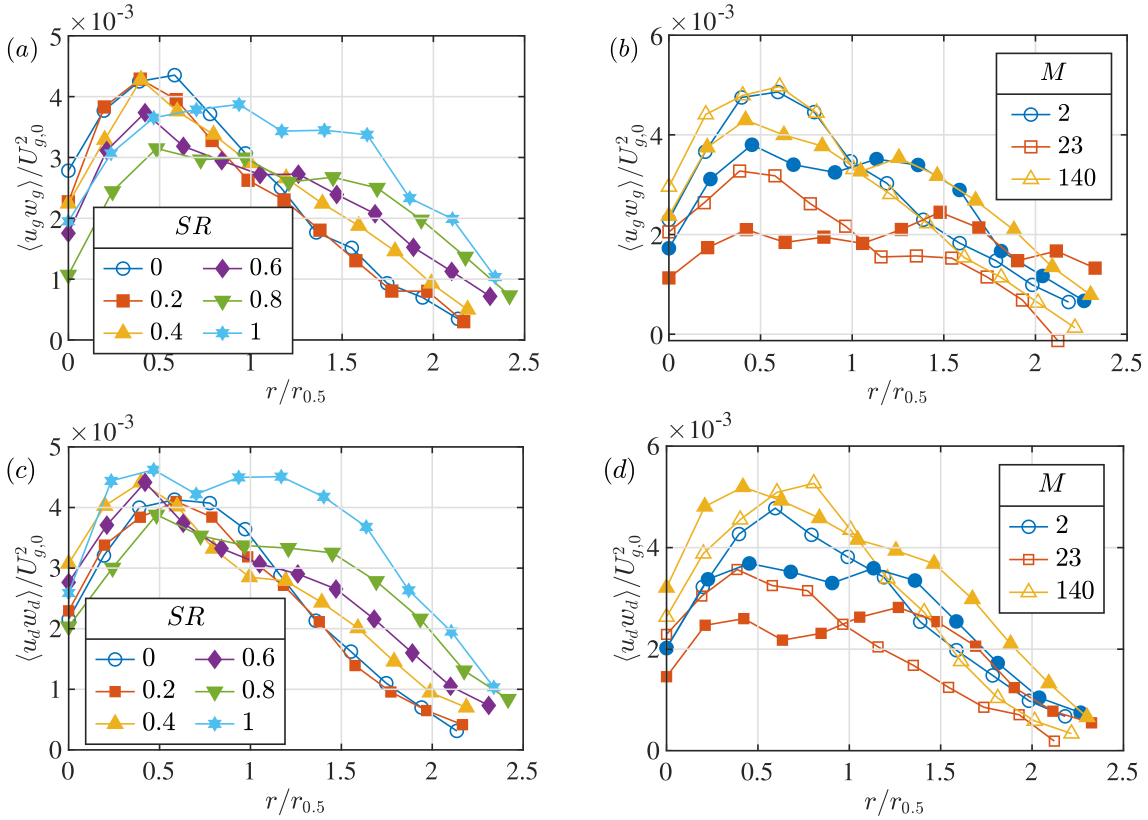

Fig. 12 Radial profiles of the covariance between the axial and radial fluctuating velocities for the gas phase (**a**, **b**) and droplets larger than 10 μm (**c**, **d**), measured at $x/d_g = 25$ and non-dimensionalized by the square of their centerline gas velocity, shown as a function of radius non-dimensionalized with their gas velocity half-widths. The non-swirling conditions are shown with open markers and swirling conditions are shown with filled markers. (**a**, **c**) For all SR at $Re_l = 1120$ and $We_g = 830$, and (**b**, **d**) non-swirling and swirling conditions for three M values (cases 1, 4 and 7)

the spray as We_g increases to be able to infer carrier phase turbulent quantities. Note that here increase of We_g is obtained by increase of the gas jet velocity U_J, which in turn increase the gas Reynolds number, decreasing the value of τ_η (which scales approximately as $U_J^{-3/2}$). However, due to the quadratic dependence of St_d on d, the droplet size is not reduced significantly enough to compensate for getting the required Stokes number. Therefore, there needs to be a compromise on the chosen drop size threshold used to infer the carrier flow statistics to compromise a reasonable Stoke number value and number of drops belonging to the size class.

5 Discussion

The Reynolds stress obtained from the gas phase has revealed some well-known (e.g., u'_g, $\langle u_g v_g \rangle$) and also some not so well-known (e.g., v'_g, $\langle v_g w_g \rangle$, $\langle u_g w_g \rangle$) behavior for turbulent jets such as the ones used in sprays. In addition, the covariances of the droplets obtained, and shown alongside the Reynolds stresses, can yield some qualitative insights into the spray physics through the lens of turbulent transport. They point to different geometric transformations experienced by an ensemble of droplets, called a patch here. For illustration, the reader can refer to Fig. 3 and associate for instance a patch as a region of high concentration (such as the black spot found at $(x, r) = (12, 0)d_g$ in Fig. 3c) or low concentration. The droplet covariance terms at that location inform on how that patch evolves as it travels downstream, statistically speaking. The diagonal terms are the velocity fluctuations, which inform how a patch expands or contracts in different directions and are therefore a measure of local volume fraction change associated with turbulence. The off-diagonal terms, on the other hand, reveal the tilting motions and deformations along diagonal directions of the patch. For example, $\langle u_d v_d \rangle$ can inform about the influence of the jet shear observed in the plane of visualization in Fig. 3 on the transport of a collection of droplets. These interpretations are supported by the observations in the supplementary videos

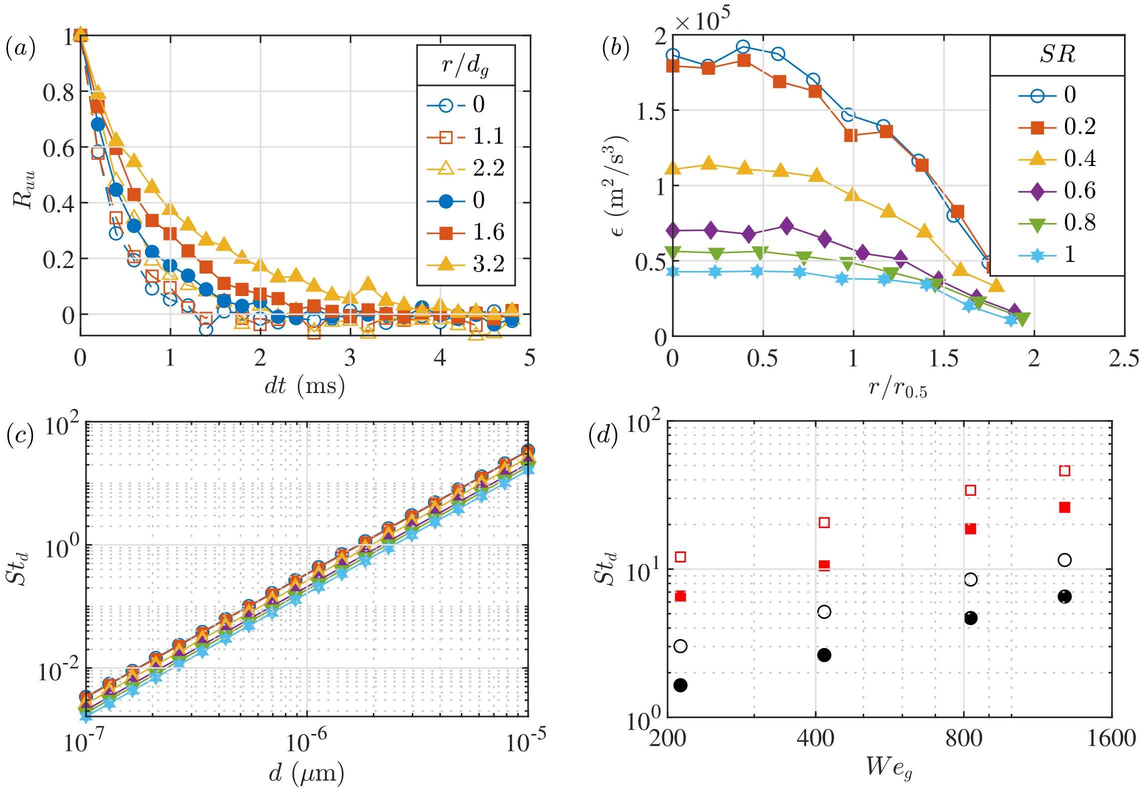

Fig. 13 Spray turbulent characteristics obtained from the small droplets ($u_g(t)$) measured at $x/d_g = 25$. Auto-correlation functions of the axial velocity fluctuations for different radial locations (**a**), and radial profiles of the turbulent dissipation rate for different swirl ratios (**b**) at $Re_l = 1120$ and $We_g = 830$. Turbulent Stokes number ($St_d = \tau_d/\tau_\eta$) calculated locally at the centerline varying with the droplet diameter (**c**), and with the gas Weber number We_g for droplet sizes $d = 5$ μm (○) and $d = 10$ μm (□) (**d**). Open and closed symbols correspond to $SR = 0$ and $SR = 0.8$, respectively

Table 2 The table of different scales for the centerline of non-swirling turbulent sprays computed considering droplets smaller than 5 μm as tracers of the gas phase for two values of the inlet gas Weber number We_g (alternatively, gas Reynolds number Re_g) when $Re_l = 1120$, and measured at $x/d_g = 25$. u_{rms} - norm of the velocity fluctuation, L - Integral length scale, T - Integral time scale, η - Kolmogorov length scale, τ_η - Kolmogorov time scale, Re_L - integral scale Reynolds number, and Re_λ - Taylor-scale Reynolds number

We_g	Re_g	u_{rms} (m/s)	L (cm)	T (ms)	η (μm)	τ_η (μs)	Re_L	Re_λ
210	52000	7	1.2	0.6	20	26	5320	282
830	102400	16	1.3	0.3	12	9	11630	418

of Sahoo et al. [49]. Therefore, the droplet covariance can be interpreted as a deformation tensor of the droplet cloud.

A brief overview of the different turbulent scales are extracted in the spray are given in Table 1 mentioned here.

The value of the Taylor-scale Reynolds number is very large, indicating fully developed turbulence for every spray conditions here. As η is of the order of 10 μm, it implies that there are a large number of droplets below η that can be treated as inertial point particles in analytical and numerical modeling (e.g, Euler-Lagrange simulations), using Maxey-Riley-Gatignol equation [56,57].

It is observed that the chosen size class to infer the gas flow turbulent characteristics, going up to 5 μm, lead to large Stokes number values, especially for $We_g = 830$. Therefore, the computation of the small-scale statistics are biased (such as the estimation of the dissipation rate ε and hence, Stokes number). Therefore, if the small-scale turbulent statistics are to be probed in such high Reynolds number sprays, specific tracers (with smaller density and/or with much smaller sizes) need to be implemented. Any (usual) liquid-based tracers will need to have a size of a fraction of a micrometer leading to large turbulent Stokes numbers. However, the integral time scale should be preserved as the Stokes number corresponding to the large-scale timescale is 0.002 or less (Table 2 show the broad scale separation found for the high Reynolds number sprays considered here). In addition, the chosen drop diameter of 5 μm is well below the integral length scale of the flow (3 orders of magnitudes below the smallest value of L). This size range is such that inertial particles display velocity fluctuation of the level of fluid, but only their acceleration statistics may be affected due to their slower response times [58,59]. At similar values of Re_λ, reaching sizes of a fraction of the integral scale is necessary to see a decrease in the particle velocity fluctuation magnitude [60].

There is one additional potential bias to mention, stressed out already in single-phase turbulence using a round jet [55]. As entrainment plays a large role in the jet's turbulence, seeding the surrounding fluid with tracers is required to faithfully capture the flow features. In the present study, the small droplets used as tracers inherently do not come from the surrounding ambient air. However, an accompanying fact of the present flow is the detrainment and reentrainment of droplets [49], which may mitigate this bias at least partially. It is important to highlight here that the calculations of turbulent dissipation given in Table 2 are based on relationships developed in homogeneous isotropic turbulence (HIT), assuming, for instance, a constant value of $C\varepsilon = 1$, which is not estimated directly here. In addition, these relationships should differ locally due to the radial transport of droplets and the carrier flow inhomogeneity and anisotropy. Taking these into account, we believe that the reported orders of magnitude of the dissipation rate values most likely underestimate the actual values.

Different investigations are required to elaborate on the characterization of turbulent swirling spray characteristics, given the multiscale and multiphysics nature of droplet formation and spray dispersion. This database forms an essential part of potential future numerical models that do not resolve the atomization process (e. g., [61]). Additionally, the Reynolds stresses presented in this work can be instrumental in numerical validation of the spray behavior through high-order statistics [62,63]. Note that the droplet covariance only informs on the magnitude of the droplet cloud's deformation tensor, but each term may be associated to a different timescale, playing a large role in the actual transport dynamics. Together, the magnitude and timescale could help build transport models for droplets in a spray.

6 Conclusion

This paper comprehensively highlights the change in the turbulence behavior between non-swirled and swirled sprays for various Re_l and We_g. The local probability distribution of different velocity components for all droplets changes its symmetry with the introduction of swirl, apart from changes in range. However, these variations are both location-dependent and condition-dependent. The centerline axial velocity of the gas phase, as identified using small droplets in the presence of spray and a hotwire anemometer in its absence, indicates that velocity fluctuations are higher in the presence of spray close to the nozzle than in the absence of a spray. This trend reverses at high axial distance and saturates for both conditions in the presence and absence of swirl. It is also observed that while the gas phase axial velocity fluctuations exhibit a self-similar behavior in the presence and absence of swirl, the large droplets deviate from this trend when the swirling intensity is low. The radial profiles of the axial velocity fluctuation u' show off-center maxima, to the exception of non-swirling conditions at high gas-to-liquid dynamic pressure ratio M. While the droplet fluctuations of the radial velocity v' for gas decrease with an increase in the swirl ratio, all conditions have a centered maximum in the radial profiles apart from low-swirling high M conditions.

The Reynolds stress component $\langle uv \rangle$ is observed to be self-similar for the gas phase independently of Re_l, We_g, and SR. However, for the big droplets, the maxima of the values are observed to increase with swirl, and the location of the maxima is observed to move closer to the axis of the spray. The Reynolds stress component $\langle v_g w_g \rangle$ is observed to decrease with the increase in r for all conditions, apart from swirling low M conditions. This highlights that the non-swirled gas jet suffers from instabilities that leads to the breaking of the axisymmetry when considering high-order statistics. For big droplets, the radial profiles become flatter, and a steady increase in their values was observed with an increase in the swirl ratio. Similarly, for the Reynolds stress component $\langle uw \rangle$, deviations were also observed due to swirl at high r for both the gas phase and the big droplets.

Further investigations were conducted on the auto-correlation function of the small droplets axial fluctuating velocity at different radial locations. These results indicated that the integral time scale increases with both swirl and radial distances. Consequently, the dissipation rate estimated using scalings from turbulent phenomenology has the reverse behavior with radius and swirl ratio. An investigation into the turbulent Stokes number computed with the Kolmogorov time scale revealed that although the droplets produced by the spray are suitable for large-scale characterization of the gas phase, they are not responsive enough to infer the carrier phase small-scale turbulent statistics. Furthermore, this evaluation of a local turbulent Stokes number shows that even using typical small tracers for gas flows (e. g., smoke, oil droplets), their size that is typically 1 μm will lead to Stokes number values around unity.

Acknowledgements This research was funded, in whole or in part, by the Agence Nationale de la Recherche under grant number ANR-22-CE30-0003-01. A CC-BY 4.0 public copyright license has been applied by the authors to the present document and will be applied to all subsequent versions up to the Author Accepted Manuscript arising from this submission, in accordance with the grant's open access conditions. The French Space Agency (CNES), through the GDR MFA is acknowledged for the financial support that contributed to building the experimental setup.

Funding This research was funded, in whole or in part, by the Agence Nationale de la Recherche under grant number ANR-22-CE30-0003-01. The French Space Agency (CNES), through the GDR MFA is acknowledged for the financial support that contributed to building the experimental setup.

Declarations

Author contributions S.K.S conducted the experiments, carried out the analysis, prepared the initial manuscript. N.M. conceptualized, reviewed the manuscript.

Data availibility The data that support the findings of this study are available from the corresponding author upon request.

Conflict of interest The authors do not have any Conflict of interest to declare.

References

1. Hardalupas, Y., Taylor, A., Whitelaw, J.H.: Velocity and size characteristics of liquid-fuelled flames stabilized by a swirl burner. Proceed. Royal Soc. London Math. Phys. Sci. **428**(1874), 129–155 (1990)
2. Singh, G., Juddoo, M., Kourmatzis, A., Dunn, M., Masri, A.: Heat release zones in turbulent, moderately dense spray flames of ethanol and biodiesel. Combust. Flame **220**, 298–311 (2020)
3. Ünal, A.: Liquid break-up in gas atomization of fine aluminum powders. Metall. Trans. B **20**, 61–69 (1989)
4. Qaddah, B., Chapelle, P., Bellot, J.P., Jourdan, J., Kewalramani, G., Deborde, A., Hammes, R., Rimbert, N.: Primary and secondary breakup of molten ti64 in an eiga atomizer for metal powder production. Powder Technol. **438**, 119665 (2024)
5. Muliadi, A., Sojka, P.E.: A review of pharmaceutical tablet spray coating. Atomization and Sprays **20**(7) (2010)
6. Rajamanickam, K., Basu, S.: Insights into the dynamics of spray-swirl interactions. J. Fluid Mech. **810**, 82–126 (2017)
7. Lasheras, J.C., Hopfinger, E.: Liquid jet instability and atomization in a coaxial gas stream. Annu. Rev. Fluid Mech. **32**(1), 275–308 (2000)
8. Marmottant, P., Villermaux, E.: On spray formation. J. Fluid Mech. **498**, 73–111 (2004)
9. Dumouchel, C.: On the experimental investigation on primary atomization of liquid streams. Exp. Fluids **45**(3), 371–422 (2008)
10. Delon, A., Cartellier, A., Matas, J.-P.: Flapping instability of a liquid jet. Phys. Rev. Fluids **3**(4), 043901 (2018)
11. Matas, J.-P., Delon, A., Cartellier, A.: Shear instability of an axisymmetric air-water coaxial jet. J. Fluid Mech. **843**, 575–600 (2018)
12. Kumar, A., Sahu, S.: Large scale instabilities in coaxial air-water jets with annular air swirl. Physics of Fluids **31**(12) (2019)
13. Charalampous, G., Hadjiyiannis, C., Hardalupas, Y.: Proper orthogonal decomposition of primary breakup and spray in co-axial airblast atomizers. Physics of Fluids **31**(4) (2019)
14. Tolfts, O., Deplus, G., Machicoane, N.: Statistics and dynamics of a liquid jet under fragmentation by a gas jet. Phys. Rev. Fluids **8**(4), 044304 (2023)
15. Sahu, S., et al.: Analysis of droplet clustering in air-assist sprays using voronoi tessellations. Physics of Fluids **30**(12) (2018)
16. Manish, M., Sahu, S.: Droplet clustering and local spray unsteadiness in air-assisted sprays. Exp. Thermal Fluid Sci. **100**, 89–103 (2019)
17. Patil, S., Sahu, S.: Air swirl effect on spray characteristics and droplet dispersion in a twin-jet crossflow airblast injector. Physics of Fluids **33**(7) (2021)
18. Huck, P.D., Osuna-Orozco, R., Machicoane, N., Aliseda, A.: Spray dispersion regimes following atomization in a turbulent co-axial gas jet. J. Fluid Mech. **932**, 36 (2022)
19. Fong, K.O., Xue, X., Osuna-Orozco, R., Aliseda, A.: Gas-liquid coaxial atomization with swirl in high-pressure environments. Int. J. Multiph. Flow **174**, 104767 (2024)
20. Acharya, A.S., Deevi, S., Dhivyaraja, K., Tangirala, A.K., Panchagnula, M.V.: Spatio-temporal microstructure of sprays: data science-based analysis and modelling. J. Fluid Mech. **912**, 19 (2021)
21. Sahu, S., Hardalupas, Y., Taylor, A.: Droplet-turbulence interaction in a confined polydispersed spray: effect of droplet size and flow length scales on spatial droplet-gas velocity correlations. J. Fluid Mech. **741**, 98–138 (2014)
22. Kumar, A., Sahu, S.: Influence of nozzle geometry on primary and large-scale instabilities in coaxial injectors. Chem. Eng. Sci. **221**, 115694 (2020)

23. Aliseda, A., Hopfinger, E.J., Lasheras, J.C., Kremer, D., Berchielli, A., Connolly, E.: Atomization of viscous and non-newtonian liquids by a coaxial, high-speed gas jet experiments and droplet size modeling. Int. J. Mult. Flow **34**(2), 161–175 (2008)
24. Osuna-Orozco, R., Machicoane, N., Huck, P.D., Aliseda, A.: Feedback control of coaxial atomization based on the spray liquid distribution. Atomization and Sprays **29**(6) (2019)
25. Osuna-Orozco, R., Machicoane, N., Huck, P.D., Aliseda, A.: Effect of electrostatic forcing on coaxial two-fluid atomization. Phys. Rev. Fluids **7**(7), 074301 (2022)
26. Osuna-Orozco, R., Machicoane, N., Huck, P.D., Aliseda, A.: Feedback control of the spray liquid distribution of electrostatically assisted coaxial atomization. Atomization and Sprays **30**(1) (2020)
27. Baillot, F., Blaisot, J.-B., Boisdron, G., Dumouchel, C.: Behaviour of an air-assisted jet submitted to a transverse high-frequency acoustic field. J. Fluid Mech. **640**, 305–342 (2009)
28. Ficuciello, A., Blaisot, J., Richard, C., Baillot, F.: Investigation of air-assisted sprays submitted to high frequency transverse acoustic fields: Droplet clustering. Physics of Fluids **29**(6) (2017)
29. Hinterbichler, H., Steiner, H., Brenn, G.: Self-similar pressure-atomized sprays. J. Fluid Mech. **889**, 17 (2020)
30. Machicoane, N., Ricard, G., Osuna-Orozco, R., Huck, P.D., Aliseda, A.: Influence of steady and oscillating swirl on the near-field spray characteristics in a two-fluid coaxial atomizer. Int. J. Multiph. Flow **129**, 103318 (2020)
31. Kaczmarek, M., Osuna-Orozco, R., Huck, P.D., Aliseda, A., Machicoane, N.: Spatial characterization of the flapping instability of a laminar liquid jet fragmented by a swirled gas co-flow. Int. J. Multiph. Flow **152**, 104056 (2022)
32. Pope, S.B.: Turbulent Flows. Cambridge University Press, New York (2000)
33. Crow, S.C., Champagne, F.: Orderly structure in jet turbulence. J. Fluid Mech. **48**(3), 547–591 (1971)
34. Panchapakesan, N.R., Lumley, J.L.: Turbulence measurements in axisymmetric jets of air and helium. part 1. air jet. Journal of Fluid Mechanics 246, 197–223 (1993)
35. Hussein, H.J., Capp, S.P., George, W.K.: Velocity measurements in a high-reynolds-number, momentum-conserving, axisymmetric, turbulent jet. J. Fluid Mech. **258**, 31–75 (1994)
36. Wygnanski, I., Fiedler, H.: Some measurements in the self-preserving jet. J. Fluid Mech. **38**(3), 577–612 (1969)
37. Kuhlman, J.M.: Variation of entrainment in annular jets. AIAA J. **25**(3), 373–379 (1987)
38. Ko, N., Chan, W.: Similarity in the initial region of annular jets: three configurations. J. Fluid Mech. **84**(4), 641–656 (1978)
39. Ko, N., Lam, K.: Flow structures of a basic annular jet. AIAA J. **23**(8), 1185–1190 (1985)
40. Billant, P., Chomaz, J.-M., Huerre, P.: Experimental study of vortex breakdown in swirling jets. J. Fluid Mech. **376**, 183–219 (1998)
41. Rajamanickam, K., Basu, S.: Insights into the dynamics of conical breakdown modes in coaxial swirling flow field. J. Fluid Mech. **853**, 72–110 (2018)
42. Machicoane, N., Osuna-Orozco, R., Aliseda, A.: Regimes of the length of a laminar liquid jet fragmented by a gas co-flow. Int. J. Multiph. Flow **165**, 104475 (2023)
43. Ricard, G., Machicoane, N., Osuna-Orozco, R., Huck, P.D., Aliseda, A.: Role of convective acceleration in the interfacial instability of liquid-gas coaxial jets. Phys. Rev. Fluids **6**(8), 084302 (2021)
44. Balachandar, S., Eaton, J.K.: Turbulent dispersed multiphase flow. Annu. Rev. Fluid Mech. **42**(1), 111–133 (2010)
45. Villafañe, L., Aliseda, A., Ceccio, S., Di Marco, P., Machicoane, N., Heindel, T.J.: 50 years of international journal of multiphase flow: Experimental methods for dispersed multiphase flows. Int. J. Multiph. Flow **189**, 105239 (2025)
46. Brandt, L., Coletti, F.: Particle-laden turbulence: progress and perspectives. Annu. Rev. Fluid Mech. **54**(1), 159–189 (2022)
47. Hardalupas, Y., Taylor, A., Whitelaw, J.H.: Velocity and particle-flux characteristics of turbulent particle-laden jets. Proceed. Royal Soc. London A Math. Phys. Sci. **426**(1870), 31–78 (1989)
48. Angriman, S., Ferran, A., Zapata, F., Cobelli, P.J., Obligado, M., Mininni, P.D.: Clustering in laboratory and numerical turbulent swirling flows. J. Fluid Mech. **948**, 30 (2022)
49. Sahoo, S.K., Wei, Y., Machicoane, N.: Spray behaviour from non-swirling to swirling gas jet in coaxial atomisation. J. Fluid Mech. **1025**, 7 (2025)
50. Tolfts, O., Rack, A., Machicoane, N.: Morphology and dynamics of the liquid jet in high-speed gas-assisted atomization retrieved through synchrotron-based high-speed x-ray imaging. Int. J. Multiph. Flow **181**, 105004 (2024)
51. Osuna Orozco, R.: Characterization and control of electrostatically assisted two-fluid coaxial atomization. PhD thesis, University of Washington (2021)
52. Dunand, A., Carreau, J.-L., Roger, F.: Liquid jet breakup and atomization by annular swirling gas jet. Atomization and sprays **15**(2) (2005)
53. Préaux, G., Lasheras, J.C., Hopfinger, E.J.: Atomization of a liquid jet by a high momentum coaxial swirling gas jet. In: Proc. 3rd Int. Conf. Multiphase Flow (1998)
54. Elghobashi, S.: On predicting particle-laden turbulent flows. Appl. Sci. Res. **52**(4), 309–329 (1994)
55. Basset, T., Viggiano, B., Barois, T., Gibert, M., Mordant, N., Cal, R.B., Volk, R., Bourgoin, M.: Entrainment, diffusion and effective compressibility in a self-similar turbulent jet. J. Fluid Mech. **947**, 29 (2022)
56. Gatignol, R.: The faxén formulae for a rigid particle in an unsteady non-uniform stokes flow. Journal de Mécanique Théorique et Appliquée (1983)
57. Maxey, M.R., Riley, J.J.: Equation of motion for a small rigid sphere in a nonuniform flow. Phys. Fluids **26**(4), 883–889 (1983)
58. Volk, R., Calzavarini, E., Leveque, E., Pinton, J.-F.: Dynamics of inertial particles in a turbulent von kármán flow. J. Fluid Mech. **668**, 223–235 (2011)
59. Qureshi, N.M., Bourgoin, M., Baudet, C., Cartellier, A., Gagne, Y.: Turbulent transport of material particles: an experimental study of finite size effects. Phys. Rev. Lett. **99**(18), 184502 (2007)
60. Machicoane, N., Zimmermann, R., Fiabane, L., Bourgoin, M., Pinton, J.-F., Volk, R.: Large sphere motion in a nonhomogeneous turbulent flow. New J. Phys. **16**(1), 013053 (2014)
61. Liu, K., Huck, P., Aliseda, A., Balachandar, S.: Investigation of turbulent inflow specification in euler–lagrange simulations of mid-field spray. Physics of Fluids **33**(3) (2021)

62. Vu, L., Machicoane, N., Li, D., Morgan, T.B., Heindel, T.J., Aliseda, A., Desjardins, O.: A computational study of a two-fluid atomizing coaxial jet: Validation against experimental back-lit imaging and radiography and the influence of gas velocity and contact line model. Int. J. Multiph. Flow **167**, 104520 (2023)
63. Kim, J., Liu, K., Balachandar, S.: Investigation of turbulent multiphase swirling jets. Acta Mech. **235**(6), 3313–3330 (2024)